

Finding White Dwarfs’ Hidden Companions using an Unsupervised Machine Learning Technique

XABIER PÉREZ-COUTO ^{1,2} MINIA MANTEIGA ^{3,2,4} AND EVA VILLAYER ^{5,6}

¹*Universidade da Coruña (UDC), Department of Computer Science and Information Technologies,
Campus de Elviña s/n, 15071, A Coruña, Galiza, Spain*

²*CIGUS CITIC, Centre for Information and Communications Technologies Research,
Universidade da Coruña, Campus de Elviña s/n, 15071 A Coruña, Galiza, Spain*

³*Universidade da Coruña (UDC), Department of Nautical Sciences and Marine Engineering,
Paseo de Ronda 51, 15011, A Coruña, Galiza, Spain*

⁴*AIRExS, CITIC/UDC, Unidad Asociada al Instituto de Astrofísica de Andalucía, CSIC*

⁵*Instituto de Astrofísica de Canarias, 38200 La Laguna, Tenerife, Spain*

⁶*Universidad de La Laguna (ULL), Astrophysics Department,
38206 La Laguna, Tenerife, Spain*

ABSTRACT

White dwarfs (WD) with main-sequence (MS) companions are crucial probes of stellar evolution. However, due to the significant difference in their luminosities, the WD is often outshined by the MS star. The aim of this work is to find hidden companions in Gaia’s sample of single WD candidates. Our methodology involves applying an unsupervised machine learning algorithm for dimensionality reduction and clustering, known as Self-Organizing Map (SOM), to Gaia BP/RP (XP) spectra. This strategy allows us to naturally separate WDMS binaries from single WDs from the detection of subtle red flux excesses in the XP spectra that are indicative of low-mass MS companions. We validate our approach using confirmed WDMS binary pairs from the SDSS and LAMOST surveys, achieving a precision of $\sim 90\%$. Applying our SOM to 90,667 sources, we identify 993 WDMS candidates, 801 of which have not been previously reported in the literature. If confirmed, our sample will increase the known WDMS binaries by 20%, making it a valuable source for stellar evolution studies. Additionally, we use the Virtual Observatory Spectral Energy Distribution Analyzer (VOSA) tool to further refine and parameterize a “golden sample” of 136 WDMS candidates through multi-wavelength photometry and a two-body Spectral Energy Distribution fitting. These high-confidence WDMS binaries are composed by low-mass WDs ($\sim 0.41M_{\odot}$), with cool MS companions (~ 2800 K). Finally, 13 systems exhibit periodic variability consistent with eclipsing binaries, making them prime targets for further follow-up observations.

Keywords: white dwarfs — binaries — methods: data analysis — catalogs

1. INTRODUCTION

It is well established that the binary fraction of stars is highly dependent on the stellar mass, ranging from 30% for M-type stars (Winters et al. 2019) to 70% for O and B-type stars (Sana et al. 2014; Moe & Di Stefano 2017), with a mean incidence of 50% for solar-type stars (Raghavan et al. 2010).

The more massive star in the pair will evolve faster and, if it is a low-to-intermediate-mass star ($\lesssim 8 M_{\odot}$), it will eventually become a white dwarf (WD, Iben et al. (1997)) forming a WD plus main-sequence (MS) star binary (hereafter, WDMS). Given the very predictable cooling age of the WDs, WDMS binary pairs

are excellent cosmic clocks that have been used to study fundamental astrophysical parameterizations such as the age–metallicity relation (Rebassa-Mansergas et al. 2021a), the initial -to- final mass (Zhao et al. 2012), and the mass-radius relation (Raddi et al. 2025).

Different outcomes are expected for the WDMS binary depending on the orbital separation. In wide orbits pairs, the MS companion evolves independently eventually leading to the formation of a WD–WD binary. Conversely, close WDMSs are susceptible to undergo mass transfer episodes, potentially leading to Cataclysmic Variables (CVs; Parsons et al. 2013; Sun et al. 2021), Novae, Symbiotic, and Type Ia Supernovae (SNe)

(Wang & Han 2012), essential tools in cosmological and stellar evolution studies (Leibundgut & Sullivan 2018).

The most extensive samples of WDMS to date are those obtained by the Sloan Digital Sky Survey (SDSS, see e.g. Rebassa-Mansergas et al. 2016) and the Large Sky Area Multi-Object Fiber Spectroscopic Telescope (LAMOST, see e.g. Ren et al. 2018) with a total of 4100 WDMSs. However, both surveys exhibit certain observational biases against cool WDMS, resulting in an apparent absence of systems with $T_{eff} < 10,000\text{K}$.

Several studies have demonstrated the feasibility of automatically identifying WDMS binaries using machine learning techniques with promising accuracy (around 80% using Random Forest; see Echeverry et al. 2022), and successfully detecting candidates in open clusters with Support Vector Machines (SVM; Grondin et al. 2024). Kao et al. (2024) in particular, identified an isolated group of 1,096 WDMS candidates by using a Uniform Manifold Approximation and Projection (UMAP) through the largest white dwarf catalog available to date. Recently, we have used Self-Organizing Maps (SOMs; Kohonen 1982), an unsupervised neural network-based algorithm to find polluted WD candidates based on Gaia XP spectra (Pérez-Couto et al. 2024).

In this work, we will use a similar methodology to that used in Pérez-Couto et al. (2024) to identify MS companions in WD spectra from the catalog of Gentile-Fusillo et al. (2021). This catalog is built using color-magnitude and astrometric cuts to prioritize single WDs. Therefore, any secondary companion to a WD in the sample is expected to be a low-mass, late-type M dwarf or even a brown dwarf, as its presence is not expected to significantly affect the photometry or astrometry of the WD.

The paper is organized as follows: in Section 2, we describe the data used and the SOM learning process, in §3 we apply the method to the data and discuss the results. Finally, in §4 we summarize our main findings and present the conclusions of the paper.

2. METHODOLOGY

The Gaia Mission (Gaia Collaboration 2023) has provided, in its Third Data Release (DR3), high-quality astrometric data and photometry from the Blue (BP) and Red Photometers (RP) for 1460 million sources of our Galaxy. This extensive dataset has been instrumental in identifying new WDMS by using the Gaia G , G_{BP} , and G_{RP} Color Magnitude Diagram (CMD) and Virtual Observatory (VO) tools. In particular, the Virtual Observatory Spectral Energy Distribution An-

alyzer (VOSA¹, Bayo et al. 2008) allowed Rebassa-Mansergas et al. (2021b) to find 97 new WDMS and parameterize their stellar properties.

In addition to the BP/RP photometry, Gaia published low-resolution ($R \approx 70$) BP/RP spectra (hereafter, XP spectra) for about 220 million sources (De Angeli et al. 2023). Instead of flux units per wavelength unit, each XP spectrum is given as an array of 110 coefficients of a series of Hermite basis functions (55 for BP and 55 for RP). Given the infeasibility of visually inspecting such an extensive data set, numerous studies have employed machine learning (ML) algorithms to mine the data in the search and classification of WD (García-Zamora et al. 2023; Vincent et al. 2024; Kao et al. 2024; Pérez-Couto et al. 2024).

Self-Organizing Maps (SOMs; Kohonen 1982), is an unsupervised neural network-based algorithm that combines either dimensionality reduction—to project the XP coefficients in a two-dimensional grid map—and cluster—to group similar elements together in the same neuron—. The power of this dual technique demonstrates that SOMs are a useful artificial intelligence tool for object classification in various fields of astrophysics (see e.g. Torres et al. 1998; Naim et al. 2009; Ordoñez-Blanco et al. 2010; Geach 2012; Way and Klose 2012; Fustes et al. 2013a,b; Carrasco and Brunner 2014; Dafonte et al. 2018; Álvarez et al. 2022; Pérez-Couto et al. 2024).

2.1. Input data

The initial sample is based on the Gentile-Fusillo et al. (2021) catalog, where a large sample of WD candidates is selected first by imposing the following cut in the Gaia CMD:

$$G_{abs} > 6 + 5 \times (G_{BP} - G_{RP}), \quad (1)$$

a `parallax_over_error > 1` and several additional quality cuts to discard bad astrometric solutions up to a final sample size of 1.3 million sources.

This color cut is indeed not the most effective way of identifying a large number of WDMS binaries, as it excludes WDs situated in the CMD between the WD locus and the MS branch—a region above which approximately 90% of WDMS binaries are expected to be found, according to recent population synthesis simulations (Rebassa-Mansergas et al. 2021b; Santos-García et al. 2025)—. Nevertheless, we adopt this color cut in the present study, which specifically focuses on the WD region. This approach ensures that any detected companion has low emission, as the WD dominates, making

¹ <http://svo2.cab.inta-csic.es/theory/vosa/>

very low-mass companions, such as M stars or brown dwarfs, the most likely candidates.

Some astrometric cuts used in the [Gentile-Fusillo et al. \(2021\)](#) catalog such as the Renormalized Unit Weight Error (RUWE) < 1.1 , `ipd_gof_harmonic_amplitude` < 1 , or `astrometric_excess_noise_sig` < 2 efficiently clean the sample from the majority of astrometric contaminants (among them, many unresolved binaries) ([Belokurov et al. 2020](#)). This, in conjunction with the fact that they are unresolved despite their proximity, makes any WDMS binary found in their catalog to be a very close binary.

In [Gentile-Fusillo et al. \(2021\)](#), the authors computed a probability of an object being a WD (P_{WD}). This probability is determined using a reference dataset of 22,998 spectroscopically confirmed WDs and 7124 contaminants identified through visual inspection in the SDSS. These datasets are modeled as normalized 2D Gaussian distributions, producing distinct density maps for WDs and contaminants. The P_{WD} for each candidate is calculated by integrating its CMD Gaussian representation with a map formed by taking the ratio of the WD density map to the combined density of both WDs and contaminants.

The definition of contaminant used in [Gentile-Fusillo et al. \(2021\)](#) included WDMS binaries, and hence a probability filter of, for instance, $P_{WD} > 0.9$, would exclude the majority of contaminants such as QSOs or Galaxies, but also most of the WDMS we aim to discover. For this reason, we will not use the P_{WD} in the following.

In contrast, we only consider as contaminants those sources with the SDSS spectral class “QSO”, “GALAXY”, and “STAR”. The “Unreli” (for unreliable) and “UNKN” (for unknown) sources in the Gaia-SDSS sample of [Gentile-Fusillo et al. \(2021\)](#) were discarded from the sample since we are not confident to confirm if they are WDs or contaminants. This leaves us with 26,423 SDSS confirmed WDs (either single or binary sources) and 4588 contaminants.

Subsequently, we use a parallax ($\bar{\omega}$) over error ($\sigma_{\bar{\omega}}$) (or $\bar{\omega}/\sigma_{\bar{\omega}} > 10$) that will ensure a more precise G_{abs} , and therefore a more reliable location in the CMD. Additionally, we have included these additional filters to ensure the quality of XP spectra:

i) `visibility_periods_used > 10`, where each visibility period is a group of observations separated from the next by at least 4 days, so that only those sources that were astrometrically well observed are retained ([Lindegren et al. 2018](#)).

ii) `(phot_bp_n_obs > 10) & (phot_rp_n_obs > 10)`, refer to the minimum number of CCD transits for BP and RP spectra, respectively, following the recommen-

dations set forth by [Andrae et al. \(2023\)](#) to ensure an adequate signal-to-noise ratio (S/N) for subsequent spectral analysis.

iii) `|phot_bp_rp_excess_factor_corrected| < 5 x sigma_excess_factor` ensures that the photometry of G_{BP} , G_{RP} , and G is consistent and free from contamination from external sources in the same field of view, as elucidated by [Riello et al. \(2021\)](#)

We obtained the Gaia XP spectra for this sample using the DataLink Gaia tool (available at <https://www.cosmos.esa.int/web/gaia-users/archive/datalink-products>) through the `astroquery` Python package ([Ginsburg et al. 2019](#)).

Finally, a S/N > 10 filter was applied through the coefficients. The S/N for both BP and RP spectra was calculated by taking the ratio between the \mathcal{L}_2 norm of the BP (RP) array of coefficients and the \mathcal{L}_2 norm of the array of BP (RP) coefficient uncertainties. As a result, we obtained an initial sample for our study comprising a total of 90,667 sources. Moreover, the SDSS confirmed WD sample has

To roughly estimate the contaminant ratio in our sample, as well as the effectiveness of the $\bar{\omega}/\sigma_{\bar{\omega}}$ filter in discarding them, we show in Figure 1b the Gaia CMD with the SDSS confirmed WDs and contaminants that meet the above filters in blue and red, respectively. However, in the CMD of the left (Figure 1a) we relax the parallax-over-error filter up to the original value in [Gentile-Fusillo et al. \(2021\)](#): $\bar{\omega}/\sigma_{\bar{\omega}} > 1$, while in the right (Figure 1b) we show the resulting CMD for $\bar{\omega}/\sigma_{\bar{\omega}} > 10$.

As illustrated in Figure 1, the image on the right is visibly more pristine and devoid of contaminants. Indeed, the contaminant fraction has been reduced from 7.5% (2074 contaminants) to 0.9% (112 contaminants), indicating that the input sample of the SOM is unlikely to contain a contamination level greater than 1%.

2.1.1. Reference catalogs

Despite the unsupervised nature of the classification process, which does not rely on a training dataset, spectroscopically confirmed WDMS spectra are required as a reference to label the final clusters. As a baseline, we rely on the Montreal White Dwarf Database² (MWDD), which is so far the most complete catalog of WDs based on more than 200 references from the literature ([Dufour et al. 2016](#)), containing information about each WD such as its spectral type or binarity. As of January 30th, 2025, it contains information for 144,800 WDs. Most of them also belong to the catalog of [Vincent et al. \(2024\)](#) which is an automatic classification of Gaia DR3 XP

² <https://montrealwhitedwarfdatabase.com>

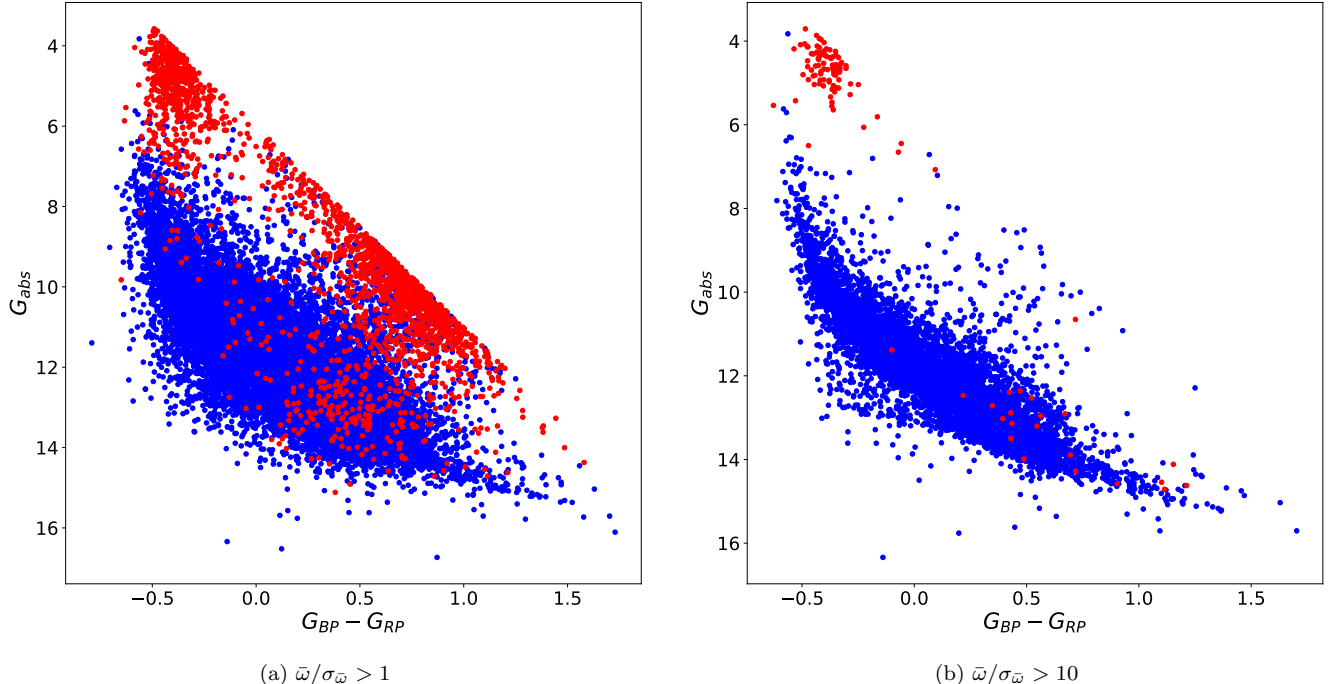


Figure 1. SDSS confirmed vs contaminants CMD with $\bar{w}/\sigma_{\bar{w}} > 1$ (left) and $\bar{w}/\sigma_{\bar{w}} > 10$ (right).

spectra based on gradient-boosted decision trees. Despite the great performance shown by their method, their classification is still based on Gaia low-resolution spectra, and thus it is a catalog of WD candidates instead of confirmed WDs.

Therefore, we decided to ignore sources with only low-resolution spectra in order to keep our reference sample of confirmed WDs as clean as possible. To this end, we discarded those sources included in the Vincent et al. (2024) catalog if they have only one available optical spectrum. For the rest of the MWDD we used all the sources with at least one available spectrum and a confirmed spectral type. We did not include sources with subdwarf (sdO, sdB, ...) spectra.

From this set, we selected as WDMS sources those with the “WDMS” binarity flag, resulting in 2849 sources. We also included some sources from the MWDD without a positive binarity flag but with a spectral type containing one of the following strings: ‘+M’, ‘+dM’, ‘+K’, ‘+G’, or ‘+F’, which indicate the presence of an MS companion in the source’s spectra. This resulted in an updated WDMS count of 3246, of which 377 have XP spectra available and that passed the filters described in Section 2.1.

We also cross-matched this MWDD WDMS sample with the largest WDMS catalogs up to date: the SDSS DR12 WDMS spectroscopic catalog (Rebassa-Mansergas et al. 2010, 2012, 2013, 2016) and the LAM-

OST DR5 catalog (Ren et al. 2014, 2018). As a result, 14 SDSS WDMS that are not classified by the MWDD as binaries have been added, as well as 19 LAMOST WDMS. This resulted in a final WDMS sample of 406 sources (4 sources were duplicated) that will be used as a reference in the labeling process of the SOM.

The remaining MWDD sources that are not included in the WDMS binary sample and that do not correspond to any other type of binarity (i.e., those with an empty binarity field in the MWDD, and a spectral type without a ‘+’ sign) are designated as single WD sources (13,479 sources), and the remaining sources in our initial sample (76,782 sources) are considered candidates in the following.

2.2. Self-Organizing Maps

While most unsupervised machine learning techniques are either utilized for dimensionality reduction (e.g. t-SNE, UMAP) or clustering (e.g. K-means, DBSCAN), SOMs integrate both applications within a single neural network-based algorithm. Indeed, given a high-dimensional nonlinear data set (in our case, constructed from arrays of 110 coefficients per spectrum), the SOM projects each element on a two-dimensional map, where analogous elements are assigned to the same neuron. Moreover, neurons with similar subpopulations are also grouped in the map, while very different subpopulations are highly distanced. This results in preserving the topology order, allowing for the recognition of pat-

terns in the data. Furthermore, the clustering of neurons into closed groups allows the accurate delineation and classification of these populations.

Once the dimensions of the map, $M \times N$ have been established, the learning process starts with a random initialization of the weight, $\mathbf{w}_{m,n}$, of each neuron, $\mathbf{z}_{m,n}$. Each $\mathbf{w}_{m,n}$ is a random array of 110 elements. After that, the first iteration takes each XP spectrum, \mathbf{x}_i , and looks for the winner neuron or Best Matching Unit (BMU), $\mathbf{z}_{m,n}$, by minimizing the distance (for example, the Euclidean distance) between \mathbf{x}_i and $\mathbf{w}_{m,n}$ is the minimum possible among all weights. Subsequently, an iterative process updates the weights at a given learning rate (h_0) that decrease over time, and following a neighborhood function that ensures the preservation of the topology. This neighborhood function (usually a Gaussian) is governed by a parameter ν that defines the initial spread of the neighborhood of each neuron.

The learning process ends after a maximum number of iterations, n_{max} , or when the weights do not change significantly (Kohonen 1982). Finally, each neuron (and thus the candidates that fell into it) receives the label corresponding to the majority class, taking as a reference the sources with a confirmed classification.

The SOM implementation used in this work is the Python MiniSom³ library for its ease of use and flexibility in hyperparameter configuration (Vettigli 2018). In the following, we will assume an squared map, $M = N$ (for simplicity and because the total number of neurons is much more crucial than their distribution)

Subsequently, to choose the best hyperparameters for the SOM (namely, the map size N^2 , ν , h_0 , and n_{max}) we implemented a grid search process, assuming for simplicity a squared map ($N = M$) with $N \in \{5, 6, 7, 8\}$; $\nu \in [0.5, 1.5]$ and $h_0 \in [0.1, 1.0]$, both in steps of 0.1; and the number of iterations $n_{max} \in \{100, 500, 1000, 5000, 10000\}$.

We built the cost function, $f = f(N, \nu, h_0, n_{max})$ to minimize as a composition of three different metrics: the quantization error (QE), the topographic error (TE), and the F_1 -score.

The QE is defined as the mean distance between each element x_i and their BMU and indicates how well the SOM represents the input data (Kohonen 1982), while the TE, quantifies the fraction of input samples for which the first and second BMU neurons were not placed adjacent in the map. That is, the TE is a measure of how well the SOM preserved the topology (Kiviluoto 1996). Both QE and TE are computed with equations

(2) and (3):

$$QE = \frac{1}{n} \sum_{i=0}^n \|\text{BMU}(x_i) - x_i\|^2 \quad (2)$$

$$TE = \frac{1}{n} \sum_{i=0}^n \epsilon(x_i), \quad (3)$$

where $\epsilon(x_i) = 1$ if the first BMU(x_i) and the second BMU(x_i) are not adjacents, and $\epsilon(x_i) = 0$ otherwise.

On the other hand, the F_1 -score is defined as the harmonic mean of the precision⁴ and the recall⁵ of the classification, and calculated with the equation (4):

$$F_1 = 2 \times \frac{\text{Precision} \times \text{Recall}}{\text{Precision} + \text{Recall}}. \quad (4)$$

Therefore, to achieve a good SOM classification, we must aim to minimize QE and TE , while maximizing the F_1 -score. To do this, we expressed $f = \max\{\tilde{Q}E, \tilde{T}E, 1 - \tilde{F}_1\}$, where the symbol “ \sim ” means that those three quantities have been previously scaled with the min-max normalization, and look for the minimum in the parameter space shown above. As a result, we found the global minimum with a map size of 8×8 neurons, $\nu = 1.4$, $h_0 = 0.4$, and 5000 maximum iterations.

It is important to recognize that the effectiveness of this approach, like other distance-based algorithms, is strongly tied to the scale of the features involved (here, the XP coefficients). To obtain the best outcomes, we normalized each XP coefficient input vector by its \mathcal{L}_2 norm before starting the learning phase.

3. RESULTS

3.1. Spectral classification

We incorporated the 90,667 sources in the form of normalized XP data into the SOM with the hyperparameters defined in §2.2. The resulting map is shown in Figure 2, where confirmed WDMS binaries are plotted in orange, single WDs in blue, and candidates are invisible to enhance visualization.

As illustrated, some confirmed WDMS binaries share the same neurons as single WDs due to their XP composite spectra being entirely dominated by the WD component. Notwithstanding that, two neurons ($z_{3,0}$ and

⁴ The precision of a class is computed as $TP/(TP + FP)$, being TP the number of True Positives and FP the number of false positives. In simple terms, it provides the probability of the algorithm to be correct when assigning a class to a source,

⁵ The recall is computed as $TP/(TP + FN)$, with FN being the number of False Negatives. It indicates the ratio of sources of a given true class that are correctly classified as that class.

³ <https://github.com/JustGlowing/minisom/>

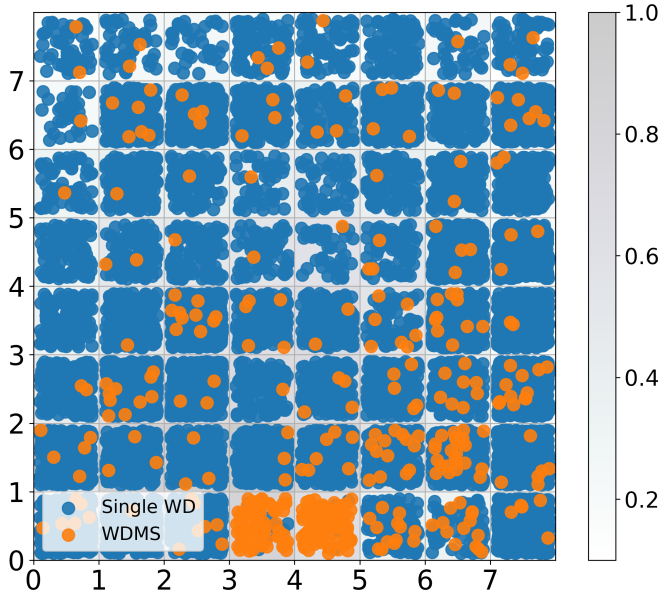


Figure 2. SOM map with our sample of 90,667 sources. WDs with a confirmed MS companion appear in orange, single WDs in blue, and candidates are invisible to enhance visualization.

$z_{4,0}$) are clearly dominated by WDMS binaries. Indeed, among the WDs fallen in neuron $z_{3,0}$, 84% are confirmed WDMS binaries; a percentage that is increased up to 92% in neuron $z_{4,0}$. Therefore, we labeled them as WDMS neurons. The other 23 neurons (having a percentage of WDMS $< 50\%$) are considered in the following as single WD neurons.

Using this labeling procedure, we can compute a confusion matrix (see Figure 3), as well as precision and recall metrics (see Table 1) to validate our methodology. The confusion matrix, C , has as rows the true labels (that is, those used as a reference, here MWDD combined with SDSS and LAMOST) and as columns the predicted labels (those assigned after the SOM clustering plus the labeling procedure described above). In this way, each cell $C_{i,j}$ contains the number of sources of the i class, classified by our SOM as belonging to the j class.

In Figure 3 we show the confusion matrix with the numbers described above in each cell, and below them the same number normalized by columns, which is equivalent to the precision. In addition to that, in Table 1 the precision, recall, and F_1 -score for each class are summarized.

As can be seen, our classification shows a very good precision (88%) in identifying WDMS binaries. On the other hand, its low recall (36%) can be explained by those WDMS binaries where the WD companion entirely dominates the SED.

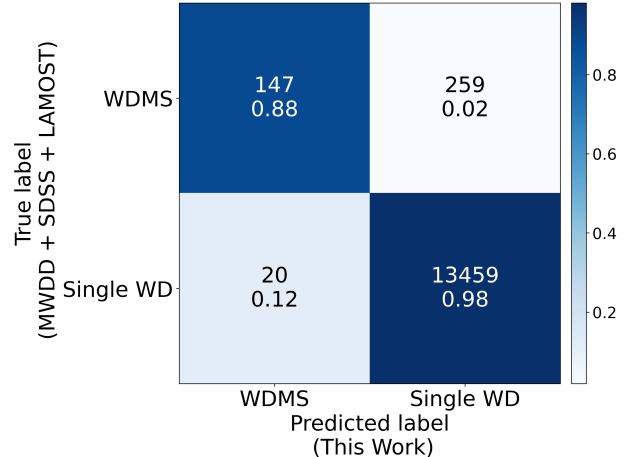


Figure 3. Confusion matrix of the binary WDMS - Single WD SOM classification.

Table 1. Precision and recall metrics for WDMS-single WD classification.

Class	Precision	Recall	F_1 -score
WDMS	0.88	0.36	0.51
Single WD	0.98	1.00	0.99

Although both $z_{3,0}$ and $z_{4,0}$ contain WDMS binaries, they are different neurons which, based on the conservation of the topology order, suggests that there is some difference between their populations. Indeed, the median, 25th and 75th percentiles of the $G_{BP} - G_{RP}$ color of the input samples in the $z_{3,0}$ neuron (hereafter, the cool WDMS neuron) is $0.47^{+0.09}_{-0.09}$ mag, while for the $z_{4,0}$ neuron (hereafter, the hot WDMS neuron) is $0.12^{+0.08}_{-0.06}$ mag. Moreover, by using the T_{eff} computed in Gentile-Fusillo et al. (2021) from the G , G_{BP} , and G_{RP} photometry assuming H -rich atmospheres, we obtained a corresponding median T_{eff} of $\sim 7500^{+800}_{-400}$ K for the cool WDMS neuron and $\sim 11,000^{+1600}_{-1000}$ K.

In general, the distribution of $G_{BP} - G_{RP}$ color across the two axes of the SOM is not expected to be irregular, since color and, correlatively, the T_{eff} are highly dependent on the spectral shape. Indeed, if we plot the $G_{BP} - G_{RP}$ color of the 90,667 sources present in the SOM, we see a smooth, non-linear gradient with the bluer sources on the left and the cooler ones on the right, as shown in Figure 4.

There are 993 sources classified as WDMS binaries (525 in the cool WDMS neuron and 468 in the hotter one), of which 846 (85%) have not yet been classified as WDMS binaries in the MWDD, SDSS, or LAMOST catalogs. These sources are therefore new WDMS binary candidates.

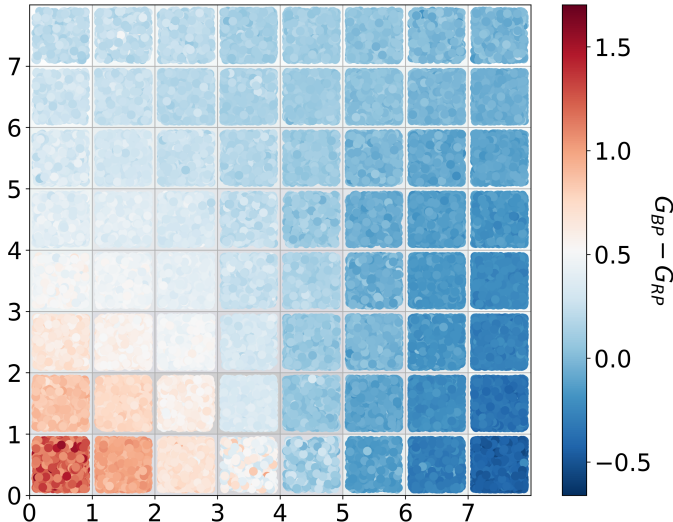


Figure 4. The SOM map displays the $G_{BP} - G_{RP}$ color of the 90,667 sources. A smooth, non-linear $G_{BP} - G_{RP}$ color gradient is shown.

In Figures 5a and 5b we show the normalized median externally-calibrated spectra of the cool and hot WDMS neurons, obtained with the `GaiaXPy`⁶ library. For comparison, we also show in green the normalized median spectra of single WD neurons, with a median $G_{BP} - G_{RP}$ color similar to that of the WDMS neurons, so that the continuum can be compared.

As can be seen in Figures 5a and 5b, both cool and hot WDMS median spectra show a clear red flux excess with respect to the single WD continuum, thus indicating the presence of an optical, late-type stellar companion in their composite spectra.

There exists the possibility that a red flux excess is due to the emission from a disk around the WD (Melis et al. 2012; Brinkworth et al. 2012; Farihi et al. 2012; Xu & Jura 2012; Hartmann et al. 2016; Rogers et al. 2024; Swan et al. 2024). We explored the possibility that the map mistook cool companions for hot disks. We put the sample of 33 WDs with disks recorded so far in the MWDD and with available XP spectra, and found that none of them fell into the binary neurons. While this does not fully exclude the possibility that some of our WDMS pairs are WDs with disks, we take as a working hypothesis that those red flux excesses are associated with MS stars due to the low number of disks observed surrounding WDs (about 1 – 3%, Wilson et al. 2019).

Furthermore, to assess the reliability of our morphological clustering, we have compared the median spectra of the 455 (391) cool (hot) WDMS binary candidates

with that of the 70 (77) cool (hot) confirmed WDMS binaries in each neuron. As shown in the same Figure 5, in both cases the median spectra of the confirmed and candidate WDMS binaries overlap almost perfectly.

3.2. WDMS eclipsing binary candidates

It is of great interest to look for variability indicators in our 993 sources' sample, since it seems reasonable to expect that the orbit of some of those systems could be aligned with the line-of-sight of Gaia, turning them into eclipsing binaries.

Indeed, 101 (10%) of our 993 WDMS candidates appear as variable sources in the Gaia Archive (`phot.variable_flag = "VARIABLE"`) so it is tempting to link that variability with the binarity clues found in their XP spectra, either because they may be CVs or eclipsing binaries. This fact is particularly enlightening given that merely 1651 sources (2%) are found to be variable within those sources in the single WD neurons.

To shed more light on this issue, we cross-matched our sample with the all-sky Gaia DR3 Eclipsing Binary catalog (`gaiadr3.vari.eclipsing.binary` table, see Mowlavi et al. 2023) that contains 2,184,477 eclipsing binary candidates obtained from *G*-band light curves cleaned and modeled to find their orbital period.

As a result, we found that 13 (1%) of our WDMS binary candidates appear in that catalog. In contrast, 100 times fewer eclipsing binary candidates are found in the single WD neurons: only 13 sources, or 0.01%. The orbital periods (P) of our 13 WDMS eclipsing binary sample are available, ranging from ~ 0.2 to ~ 1.5 days, with a median of 0.5 days. This finding suggests that their orbits are particularly close.

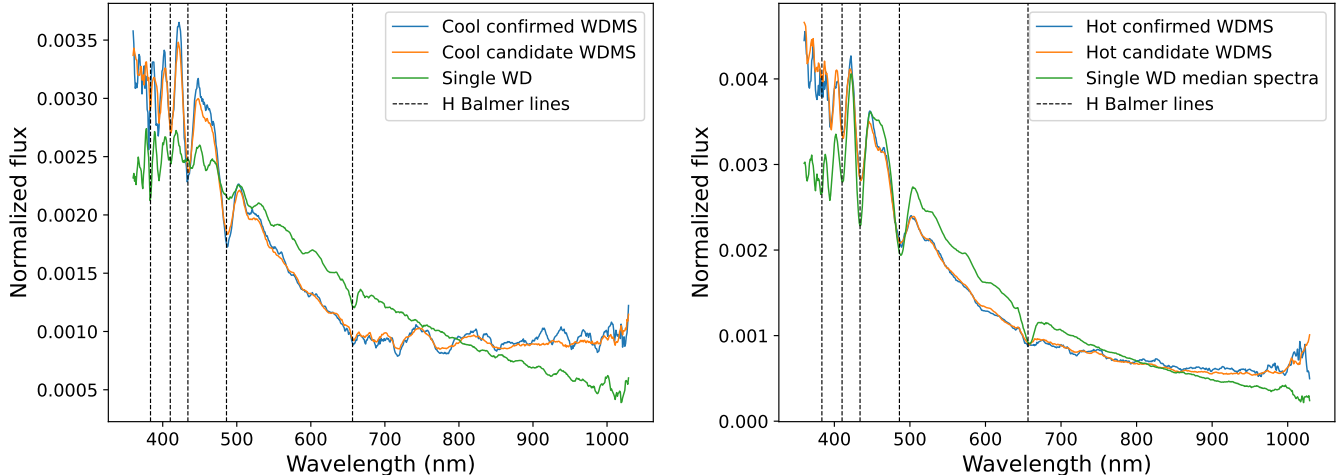
3.3. Stellar parametrization with VOSA

In order to validate our sample of WDMS candidates with external data and to estimate their astrophysical parameters, we used VOSA. This VO tool enables us to gather photometric data from major multi-wavelength astronomical surveys and to compile these data into an observational SED (Bayo et al. 2008).

This SED is subsequently used to fit the stellar parameters of the source by using any theoretical model publicly available in the literature. Furthermore, VOSA enables the implementation of a binary fit algorithm, which aims to fit two models to the SED simultaneously: one model for each companion.

To apply VOSA to our WDMS candidates, we used the following input parameters: the Gaia DR3 source ID, equatorial coordinates in J2000.0 (to calculate them from the Gaia J2016.0 epoch, we employed proper motions and parallax information in Gaia, and the `astropy`

⁶ <https://gaia-dpci.github.io/GaiaXPy-website/>



(a) Cool WDMS candidates median spectra (orange) vs cool confirmed WDMS median spectra (blue).

(b) Hot WDMS candidates median spectra (orange) vs hot confirmed WDMS median spectra (blue).

Figure 5. Comparison between the normalized median spectra of the confirmed WDMS (blue) and that of the candidates (orange) for both the cool and hot WDMS neurons. The median spectra of a single WD neuron with comparable $G_{BP} - G_{RP}$ color is included (green) so that the red flux excess can be seen.

library (Astropy Collaboration et al. 2022)), geometric distances from the catalog of Bailer-Jones et al. (2021) and the mean visual extinctions A_v calculated in Gentile-Fusillo et al. (2021).

As source catalogs for the photometric points we used the GALEX GR6/7 (Bianchi et al. 2017) in the UV range; SDSS DR12 (Alam et al. 2015), Gaia DR3 (Gaia Collaboration 2023), and Pan-STARRS DR2 (Magnier et al. 2020) in the optical; and DENIS (Epchtein et al. 1994), 2MASS (Skrutskie et al. 2006), and CatWISE2020 (Marocco et al. 2021) for the near IR (NIR). Furthermore, since we have Gaia XP spectra available for every source, we also incorporated their J-PAS synthetic photometry with GaiaXPpy (Benitez et al. 2014; Montegriffo et al. 2023). All photometry was programmatically retrieved with VOSA, except that from CatWISE2020 and J-PAS since they are not currently included in VOSA, so we loaded them manually.

Once VOSA has obtained the photometric points of each source, it automatically rejects those points bearing bad quality flags in their respective catalogs. An equivalent procedure was applied to our CatWISE2020 photometry by imposing high-quality flags ($ccf = 0000$ and $ab_flag = 00$, see Marocco et al. (2021) for further details). Moreover, we discarded any point in the overall photometry with a relative error for the flux greater than 20%, and retained only those sources with at least a point from 2MASS and CatWISE2020 photometry, to ensure NIR coverage. This last filter is highly conservative and reduces our final sample of WDMS with computed parameters (from 993 to 323 sources). However,

we consider it crucial if we want to obtain a reliable SED fit since the low-mass MS companions are expected to have their emission peak in the NIR. Furthermore, by doing so we prevent overfitting issues due to the high number of optical points mainly provided by the J-PAS synthetic photometry.

Subsequently, we fitted the resulting photometry to three distinct types of models: a single-body fit to the BT-Settl-CIFIST model (Baraffe et al. 2015) (setting $1200 \leq T_{eff}/K \leq 7000$ and $4 \leq \log g/dex \leq 5$ for MS stars); a single-body fit to the WD Koester model (Koester 2010) ($5000 \leq T_{eff}/K \leq 80,000$, and $6.5 \leq \log g/dex \leq 9.5$); and a two-body fit using both models simultaneously.

It should be noted that, although the WD Koester model assumes hydrogen-rich (DA) atmospheres, this hypothesis is more than reasonable in our work since our WDMS candidates clearly show Balmer lines, as can be seen in Figure 5.

To assess the quality of a fit, VOSA uses the visual goodness-of-fit (Vgf_b), a modified version of the reduced χ^2 in which the relative photometric errors are considered to be at least 10%, to prevent any underestimation of the uncertainties. In this way, a SED is considered well-fitted if $Vgf_b < 10 - 15$. Notwithstanding that, Nayak et al. (2024) have detected that some SEDs fittings with low Vgf_b are not always satisfactory. Moreover, a preliminary analysis of some fits in this work has shown that a $Vgf_b < 10$ is compatible with a χ^2_{red} as high as 100 or 1000. Consequently, we decided to

use $\max\{\chi_{red}^2, \text{Vgf}_b\} < 10$ as a more conservative but reliable criterion to define a good quality SED fitting.

From the sample of 323 WDMS binary candidates with available optical and NIR photometry, 137 of them shown an excellent fit to the binary WD Koester – BT-Settl SED model, according to the criteria described above. Moreover, none of our sources shown a good fit to the single BT-Settl SED, and only one source fitted well to the single WD Koester SED, with a better χ_{red}^2 and Vgf_b than for the binary SED fit, so we discarded it.

As a result, we have obtained a golden sample of 136 high-confidence WDMS binary candidates for which VOSA provides the best-fitted T_{eff} and bolometric flux (F_{bol}) for each companion.

In Figure 6 we present the calibrated XP spectra of the cool and hot WDMS neutron prototype (i.e., the source most similar to the externally-calibrated median spectra) in the left, and their VOSA binary fitted SEDs in the right.

The final WDMS binary candidates show a median, 25th, and 75th T_{eff} percentiles for the WD companion of $15,000^{+3750}_{-2500}$ K, although there is a slight difference between the median T_{eff} of hot and cool neurons (12,500 K for the cool neuron and 17,250 K for the hotter one). These values are approximately 5000 – 6000 K higher than those obtained from the T_{eff} calculated in Gentile-Fusillo et al. (2021) assuming a single WD. This discrepancy is most likely due to the fact that they only used the G , G_{BP} , and G_{RP} colors to fit their atmospheric models while we used a significantly larger set of photometric points spanning a wider wavelength range from the UV (where the emission peak in WDs is located) to the NIR.

Regarding the MS companion, the T_{eff} has a median, 25th, and 75th percentile of 2800^{+200}_{-100} K that, when translated to spectral types using the updated tables of Pecaut & Mamajek (2013), is equivalent to a median M6V type.

It is worth mentioning that there are 9 sources in which the faint companion has $T_{eff} \leq 2250$ K, compatible with a brown dwarf (BD) candidate (Pecaut & Mamajek 2013; Kirkpatrick et al. 2021). Further spectroscopic follow-up observations are planned to confirm these objects.

3.4. Stellar masses

In principle, WD masses can not be directly determined by VOSA, since the SED fitting has not enough sensitivity to $\log g$ which, furthermore, it has an uncertainty as large as 0.5 dex. Therefore, to compute the WD mass (M_{WD}) we used the evolutionary models of

Bédard et al. (2020) along with the T_{eff} and L_{bol} determined in the previous Section §3.3.

In Figure 7 we present the WD evolutionary sequences of Bédard et al. (2020) in a $L_{bol} - T_{eff}$ diagram for different masses (among $0.2M_{\odot}$ and $1.3M_{\odot}$), assuming a C/O core, He mantle, and a thick H outer layer. Over them, we plotted our 136 golden WDMS binary candidates. Subsequently, we calculated the M_{WD} for each WD by means of a linear interpolation. There are only three sources out of the convex hull of the WD evolutionary tracks, indicating that they may possess masses lower than $0.2M_{\odot}$. However, we decided to not compute M_{WD} for them to avoid extrapolated values. Moreover, we interpolated the T_{eff} and L_{bol} upper and lower values to obtain upper and lower limits of the mass.

As a result, we found that the remaining 133 WD companions have masses ranging from 0.20 to $0.77 M_{\odot}$, with a median, 25th, and 75th percentile of $0.41^{+0.09}_{-0.08} M_{\odot}$, thus revealing a population of very-low-mass WDs. Indeed, 26 sources (20% of the sample) have $< 0.3 M_{\odot}$ and are therefore considered extremely low mass (ELM) WDs.

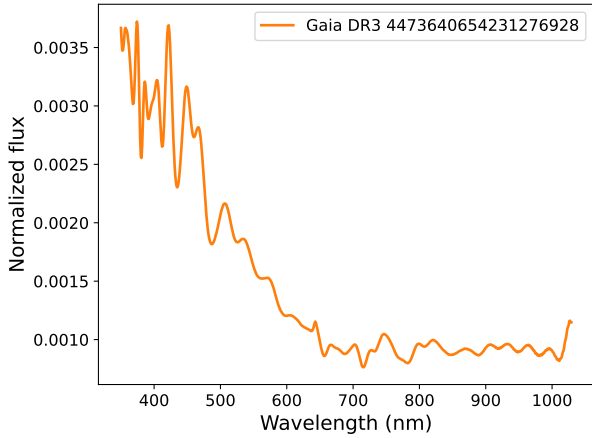
Regarding to the MS companions, we estimated their masses (M_{MS}) by means of a cubic spline interpolation of their T_{eff} through the Pecaut & Mamajek (2013) tables.

Using the masses M_{WD} and M_{MS} of four of the WDMS eclipsing binary candidates for which the orbital period is known (see §3.2) we obtained their semi-major axes, a , using the Kepler’s Third Law: $a = \sqrt[3]{(M_{WD} + M_{MS}) P^2}$. Not surprisingly, they were found to be very small, with a ranging from ~ 0.01 to ~ 0.03 au.

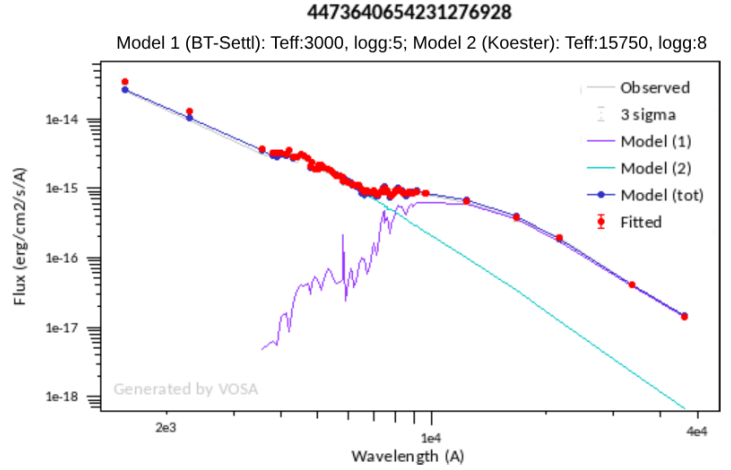
3.5. Comparison with previous works

To gain some insight into how many of our WDMS candidates are indeed new identifications, we compared them with the 100 pc volume-limited sample of Gaia EDR3 WDMS binaries from Rebassa-Mansergas et al. (2021b) (hereafter, RM21), finding three common sources. Nayak et al. (2024) (hereafter, N24) used the Gaia CMD but in combination with UV data from GALEX GR6/7, and identified 93 WDMS, two of which are in our sample, but also in RM21. None of our sources are in the catalog of WDMS binaries in open clusters of Grondin et al. (2024).

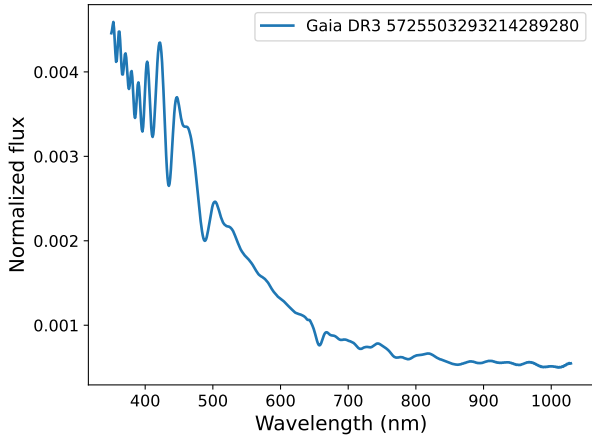
Furthermore, we compared our results with the work of Kao et al. (2024), where a UMAP allowed the authors to project the XP spectra of the high-confidence WDs from the Gentile-Fusillo et al. (2021) catalog, in a two-dimensional manifold where similar elements fall close to each other. Subsequently, they used the RUWE and



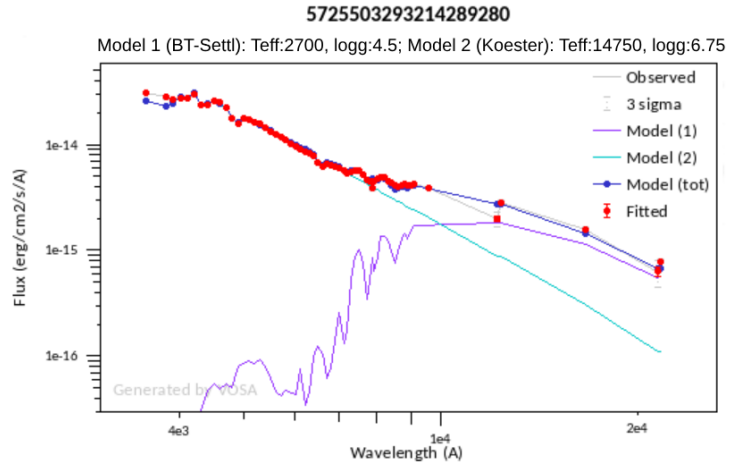
(a) Externally calibrated XP spectra of the cool WDMS prototype



(b) Photometric points found by VOSA for the cool WDMS prototype and fitted to a binary SED



(a) Externally calibrated XP spectra of the hot WDMS prototype



(b) Photometric points found by VOSA for the hot WDMS prototype and fitted to a binary SED

Figure 6. Calibrated Gaia XP spectra and two-body SED fitted for the cool (top) and hot (bottom) prototypes of the WDMS binary candidates.

a photometric scatter metric to trace the most likely position of the WDMS binaries in the UMAP. As a result, they found an island of 1096 WDMS candidates.

After finding that 368 of our WDMS are in their catalog, we plotted them in their UMAP as orange and purple triangles (corresponding to sources of our cool and hot WDMS neuron, respectively), as can be seen in Figure 8. The WDMS island found by Kao et al. (2024) is inside the red circle, where 42 sources of our cool WDMS neuron fell. Not surprisingly, the sources of the hot WDMS neuron are located on the opposite side of the UMAP. Finally, we can confidently report that at least 801 of our WDMS binaries (12 of them with eclipsing variability nature) have not been previously classified in the literature.

It should be noted that our WDMS candidates are located in the regions of the UMAP with higher values of RUWE and photometric scatter (see Figure 5 in their work), demonstrating a strong agreement between the present study and their work.

Finally, we have compared the WD mass, radius, and T_{eff} of both companions of our golden WDMS candidates with those obtained in RM21 and N24, as shown in Figure 9.

As can be seen, WDs in our sample are slightly hotter than those in N24 and RM21, respectively, although their masses and radii are quite similar to those in RM21 thus indicating that our sample belongs to a younger WD population. Moreover, they are lighter and bigger than those found in N24.

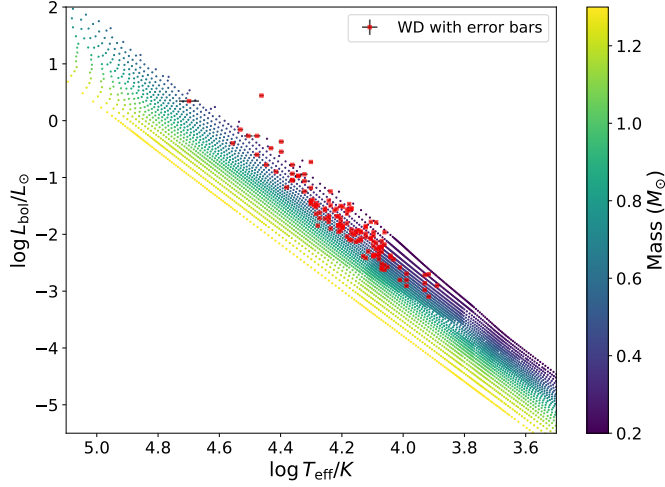


Figure 7. WD evolutionary sequences from [Bédard et al. \(2020\)](#) and the WD companions of this work

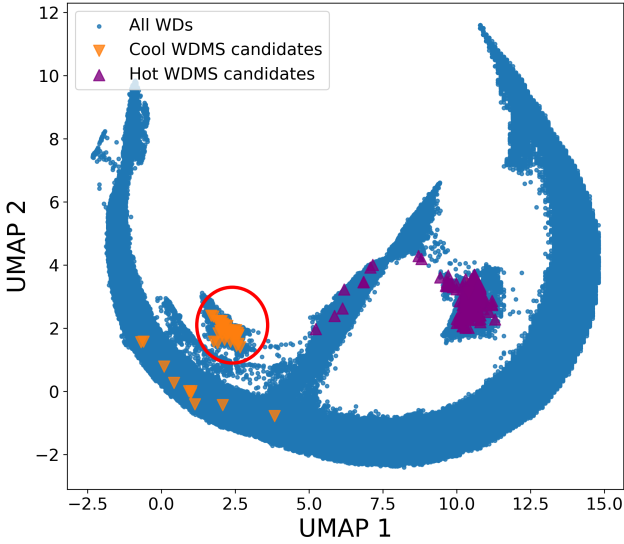


Figure 8. UMAP of [Kao et al. \(2024\)](#) with WDs in blue and our WDMS binaries in orange. The WDMS island identified by the authors is delineated as a red circle.

Regarding our MS companions, while both RM21 and N24 T_{eff} distributions follow an approximately Gaussian shape, our faint companions show a bimodal shape. Most of the sources have a mean T_{eff} aligned with that of RM21’s WDs, but slightly lower than those in N24. However, a second and smaller peak placed at its left and corresponding to the BD candidates found in Section 3.3 show that those exotic sources are mostly excluded from previous works.

Finally, during the preparation of this manuscript, [Santos-García et al. \(2025\)](#) published a comprehensive

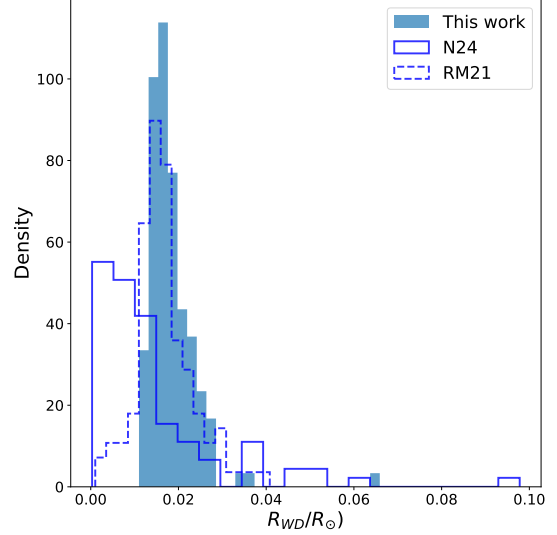
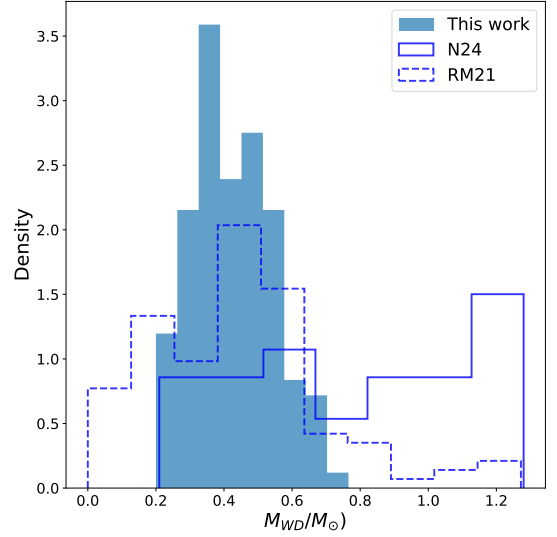
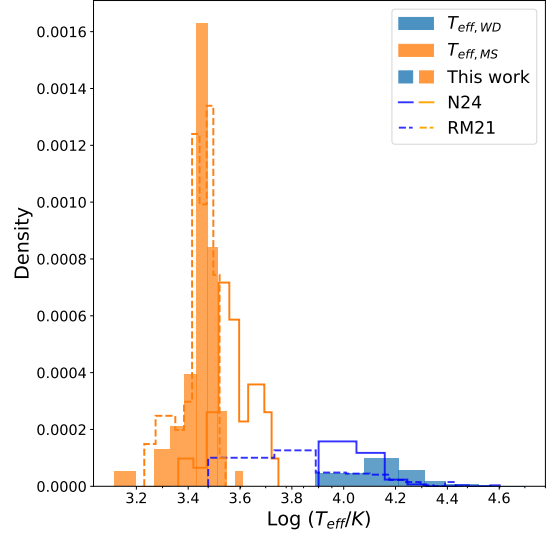


Figure 9. T_{eff} distribution for each companion in our golden sample (top), M_{WD} distribution (middle), R_{WD} distribution (bottom) and comparison with the corresponding distributions in RM21 and N24.

Table 2. Median, 25th, and 75th percentile of some stellar parameters obtained for our sample in comparison with the works of and [Rebassa-Mansergas et al. \(2021b\)](#) and [Nayak et al. \(2024\)](#)

Parameter	N24	RM21	This work
$T_{eff,WD}/K$	$11,000^{+1750}_{-1000}$	7500^{+5000}_{-2000}	$15,000^{+3750}_{-2500}$
$T_{eff,MS}/K$	3800^{+800}_{-300}	2800^{+200}_{-200}	2800^{+200}_{-100}
M_{WD}/M_{\odot}	$0.76^{+0.33}_{-0.25}$	$0.44^{+0.12}_{-0.21}$	$0.41^{+0.09}_{-0.08}$
R_{WD}/R_{\odot}	$0.010^{+0.007}_{-0.004}$	$0.016^{+0.004}_{-0.003}$	$0.017^{+0.004}_{-0.003}$

statistical study of the Gaia unresolved WDMS sample within 100 pc using population synthesis simulations. In their paper, they found that the majority of unresolved WDMS binaries are located in the main sequence ($\sim 90\%$), and in the intermediate region between the main sequence and the WD region (hereafter, the intermediate WDMS region, $\sim 10\%$). In fact, depending on the observational cuts they only expect to find between five and eight WDMS unresolved binaries within 100 pc in the WD region.

To compare our results with their conclusions we show in Figure 10 our 993 WDMS candidates plotted as blue dots in the Gaia CMD. A subset with the 15 sources that are within 100 pc are highlighted in orange. In black we show the upper boundary of the WD locus as defined in [Gentile-Fusillo et al. \(2021\)](#) (hereafter GF21; see (1)) used in this work, and in red and blue the upper and lower boundaries of the intermediate WDMS region defined in [Rebassa-Mansergas et al. \(2021b\)](#) and used in [Santos-García et al. \(2025\)](#). As can be seen, only seven WDMS candidates are located below their intermediate WDMS region, which is in excellent agreement with their study.

In summary, the WDMS candidates found in this work represent a new, different, and complementary population to that previously studied in the literature. However, follow-up observations of our candidates are necessary to confirm their binarity. If verified, our sample of 801 new WDMS binary candidates would increase the total number of known WDMS binary systems by $\sim 20\%$.

4. CONCLUSIONS

In this work, we have demonstrated the power of Self-Organizing Maps to unveil subtle regularities in the Gaia XP spectra. By combining dimensionality reduction and clustering, our SOM allowed us to identify a thousand of unresolved WDMS candidates in the [Gentile-Fusillo et al. \(2021\)](#) catalog, including 801 new candidate binaries that have not been previously classified in the literature.

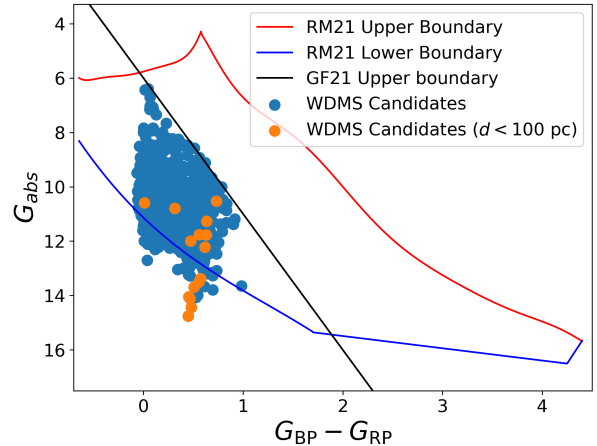


Figure 10. Gaia CMD with the 993 WDMS candidates found in this work, and the boundaries for the WD and WDMS region of [Gentile-Fusillo et al. \(2021\)](#) and [Santos-García et al. \(2025\)](#).

The analysis presented here illustrates how the SOM can successfully separate WDMS binaries from single WDs based on spectral morphology. Even though our initial sample consists of WD companions that dominate the astrometry and photometry of their systems, our SOM demonstrates an excellent precision ($\sim 90\%$) in detecting red flux excesses. While the recall can be improved, it is sufficient to recover a third of the WDMS binaries present in the input sample.

We further validated 136 sources in our sample using the VOSA tool to fit binary SEDs with external UV, optical, and NIR photometry together with independent atmospheric models. As a result, we obtained a golden sample for which individual temperatures, luminosities, radii, and masses are estimated.

Using these parameters, we characterized our sample as belonging to a population of atypical low-mass WDs that also include low-mass companions, primarily M dwarfs. A comparison with state-of-the-art WDMS catalogs shown that our method identified a complementary and previously undetected population of WDMS binaries. This highlights the potential of Gaia DR3 (and the forthcoming DR4) XP spectra combined with unsupervised learning techniques to expand the known WDMS population.

Finally, a cross-match with the Gaia DR3 eclipsing binary catalog shows that at least 13 of our candidates have periodic variability, further supporting their classification as short-period interacting binaries with separations of the order of ~ 0.01 au. This subset of systems represents promising targets for follow-up studies.

Scientific progress thrives on discussion and collaboration, and this paper is no exception. We sincerely thank the comments of our colleagues, Alberto Rebassa-Mansergas, Santiago Torres, Raquel Murillo-Ojeda, and Alejandro Santos-García during the 3rd meeting of the Iberian White Dwarf Workshop held in A Coruña in January 2025. However, any error is the sole responsibility of the authors. This work has made use of data from the European Space Agency (ESA) Gaia mission and processed by the Gaia Data Processing and Analysis Consortium (DPAC). Funding for the DPAC has been provided by national institutions, in particular, the institutions participating in the Gaia Multilateral Agreement. This work has made use of the Python package GaiaXPY, developed and maintained by members of the Gaia Data Processing and Analysis Consortium (DPAC) and in particular, Coordination Unit 5 (CU5), and the Data Processing Centre located at the Institute of Astronomy, Cambridge, UK (DPCI). This publication makes use of VOSA, developed under the Spanish Virtual Observatory (<https://svo.cab.inta-csic.es>) project funded by MCIN/AEI/10.13039/501100011033/ through grant PID2020-112949GB-I00. VOSA has been partially updated by using funding from the European Union's Horizon 2020 Research and Innovation Programme, under Grant Agreement n^o 776403 (EXOPLANETS-A). This research was funded by the Horizon Europe [HORIZON-CL4-2023-SPACE-01-71] SPACIOUS project, Grant Agreement no. 101135205, the Spanish Ministry of Science MCIN / AEI / 10.13039 / 501100011033, and the European Union FEDER through the coordinated grant PID2021-122842OB-C22. We also acknowledge support from the Xunta de Galicia and the European Union (FEDER Galicia 2021-2027 Program) Ref. ED431B 2024/21, ED431B 2024/02, and CITIC ED431G 2023/01. X.P. acknowledges financial support from the Spanish National Programme for the Promotion of Talent and its Employability grant PRE2022-104959 co-funded by the European Social Fund and E.V acknowledges funding from Spanish Ministry project PID2021-127289NB-100 is also acknowledged.

REFERENCES

- Alam, S., Albareti, F. D., Allende Prieto, C., et al. 2015, *ApJS*, 219, 12. doi:10.1088/0067-0049/219/1/12
- Álvarez, M.A., Dafonte, C., Manteiga, M. et al. 2022, *Neural Comput & Applic*, 34, 1993–2006
- Andrae, R., Fouesneau, M., Sordo, R., et al. 2023, *A&A*, 674, id.A27, 22.
- Astropy Collaboration, Price-Whelan, A. M., Lim, P. L., et al. 2022, *ApJ*, 935, 167. doi:10.3847/1538-4357/ac7c74
- Bailer-Jones, C. A. L., Rybizki, J., Fouesneau, M., et al. 2021, *VizieR Online Data Catalog*, 1352. 1/352
- Baraffe, I., Homeier, D., Allard, F., et al. 2015, *A&A*, 577, A42. doi:10.1051/0004-6361/201425481
- Bayo, A., Rodrigo, C., Barrado Y Navascués, D., et al. 2008, *A&A*, 492, 277. doi:10.1051/0004-6361:200810395
- Bédard, A., Bergeron, P., Brassard, P., et al. 2020, *ApJ*, 901, 93. doi:10.3847/1538-4357/abafbe
- Belokurov, V., Penoyre, Z., Oh, S., et al. 2020, *MNRAS*, 496, 1922. doi:10.1093/mnras/staa1522
- Benitez, N., Dupke, R., Moles, M., et al. 2014, *arXiv:1403.5237*. doi:10.48550/arXiv.1403.5237
- Bianchi, L., Shiao, B., & Thilker, D. 2017, *ApJS*, 230, 24. doi:10.3847/1538-4365/aa7053
- Brinkworth, C. S., Gänsicke, B. T., Girven, J. M., et al. 2012, *ApJ*, 750, 86. doi:10.1088/0004-637X/750/1/86
- Carrasco, K. M., Brunner, R. J. 2014, *MNRAS*, 438(4), 3409–3421
- Dafonte, C., Garabato, D., Álvarez, M.A., Manteiga, M. 2018, *Sensors*, 18, 1419
- De Angeli, F., Weiler, M., Montegriffo, P., et al. 2023, *A&A*, 674, A2
- Dufour, P., Blouin, S., et al. 2016, *arXiv:1610.00986* [astro-ph.SR]
- Echeverry, D., Torres, S., Rebassa-Mansergas, A., et al. 2022, *A&A*, 667, A144
- Epchtein, N., de Batz, B., Copet, E., et al. 1994, *Ap&SS*, 217, 3. doi:10.1007/BF00990013
- Farihi, J., Gänsicke, B. T., Steele, P. R., et al. 2012, *MNRAS*, 421, 1635. doi:10.1111/j.1365-2966.2012.20421.x
- Fustes, D., Dafonte, C., Arcay, B. et al. 2013, *Expert Syst Appl*, 40(5), 1530–1541.
- Fustes, D., Manteiga, M., Dafonte, C. et al. 2013, *A&A*, A7, 10.
- Gaia Collaboration: Vallenari, A., Brown, A.G.A., Prusti, T., et al. 2023, *A&A* 674, A1
- García-Zamora E. M., Torres S., Rebassa-Mansergas A., 2023, *A&A*, 679, A127
- Geach, J. E. 2012, *MNRAS*, 419, 2633–2645
- Gentile Fusillo, N. P., Tremblay, P.-E., Cukanovaite, E., et al. 2021, *MNRAS*, 508, 3877. doi:10.1093/mnras/stab2672
- Ginsburg, A., Sipőcz, B. M., Brasseur, C. E., et al. 2019, *AJ*, 157, 98. doi:10.3847/1538-3881/aafc33
- Grondin, S. M., Drout, M. R., Nordhaus, J., et al. 2024, *ApJ*, 976, 102. doi:10.3847/1538-4357/ad7500
- Hartmann, S., Nagel, T., Rauch, T., et al. 2016, *A&A*, 593, A67. doi:10.1051/0004-6361/201628403
- Iben I.J., Ritossa C., Garcia-Berro E., 1997, *ApJ*, 489, 772
- Kao, M. L., Hawkins, K., Rogers, L. K., et al. 2024, *ApJ*, 970, 181. doi:10.3847/1538-4357/ad5d6e
- Kirkpatrick, J. D., Gelino, C. R., Faherty, J. K., et al. 2021, *ApJS*, 253, 7. doi:10.3847/1538-4365/abd107
- Kiviluoto, K. 1996, in *Proc. Int. Conf. Neural Netw. (ICNN'96)*, Vol. 1, 294
- Koester, D. 2010, *Mem. Soc. Astron. Italiana*, 81, 921
- Kohonen, T. 1982, *Biol. Cybern.* 43, 59-69
- Leibundgut, B. & Sullivan, M. 2018, *SSRv*, 214, 57. doi:10.1007/s11214-018-0491-8
- Lindegren, L., Hernández, J., Bombrun, A., et al. 2018. *A&A*, 616, id.A2, 25
- Magnier, E. A., Schlafly, E. F., Finkbeiner, D. P., et al. 2020, *ApJS*, 251, 6. doi:10.3847/1538-4365/abb82a
- Marocco, F., Eisenhardt, P. R. M., Fowler, J. W., et al. 2021, *ApJS*, 253, 8. doi:10.3847/1538-4365/abd805
- Melis, C., Dufour, P., Farihi, J., et al. 2012, *ApJL*, 751, L4. doi:10.1088/2041-8205/751/1/L4
- Moe, M. & Di Stefano, R. 2017, *ApJS*, 230, 15. doi:10.3847/1538-4365/aa6fb6
- Montegriffo, P., Bellazzini, M., De Angeli, F., et al. 2023, *A&A*, 674, A33. doi:10.1051/0004-6361/202243709
- Mowlavi, N., Holl, B., Lecoeur-Taïbi, I., et al. 2023, *A&A*, 674, A16. doi:10.1051/0004-6361/202245330
- Naim, A., Ratnatunga, U., Griffiths, E. 2009, *ApJ Suppl Series* 111, 357
- Nayak, P. K., Ganguly, A., & Chatterjee, S. 2024, *MNRAS*, 527, 6100. doi:10.1093/mnras/stad3580
- Ordoñez-Blanco, D., Arcay, B., Dafonte, C. et al. 2010, *Lect Notes Essays Astrophys*, 4, 97–102
- Parsons, S. G., Gänsicke, B. T., Marsh, T. R., et al. 2013, *MNRAS*, 429, 256. doi:10.1093/mnras/sts332
- Pecaut, M. J. & Mamajek, E. E. 2013, *ApJS*, 208, 9. doi:10.1088/0067-0049/208/1/9
- Pérez-Couto, X., Pallas-Quintela, L., Manteiga, M., et al. 2024, *ApJ*, 977, 31. doi:10.3847/1538-4357/ad88f5
- Raddi, R., Rebassa-Mansergas, A., Torres, S., et al. 2025, *arXiv:2502.01285*. doi:10.48550/arXiv.2502.01285
- Raghavan, D., McAlister, H. A., Henry, T. J., et al. 2010, *ApJS*, 190, 1. doi:10.1088/0067-0049/190/1/1
- Rebassa-Mansergas, A., Gänsicke, B. T., Schreiber, M. R., et al. 2010, *MNRAS*, 402, 620. doi:10.1111/j.1365-2966.2009.15915.x
- Rebassa-Mansergas, A., Nebot Gómez-Morán, A., Schreiber, M. R., et al. 2011, *MNRAS*, 413, 1121. doi:10.1111/j.1365-2966.2011.18200.x
- Rebassa-Mansergas, A., Nebot Gómez-Morán, A., Schreiber, M. R., et al. 2012, *MNRAS*, 419, 806. doi:10.1111/j.1365-2966.2011.19923.x
- Rebassa-Mansergas, A., Agurto-Gangas, C., Schreiber, M. R., et al. 2013, *MNRAS*, 433, 3398. doi:10.1093/mnras/stt974
- Rebassa-Mansergas, A., Ren, J. J., Parsons, S. G., et al. 2016, *MNRAS*, 458, 3808. doi:10.1093/mnras/stw554
- Rebassa-Mansergas, A., Solano, E., Xu, S., et al. 2019, *MNRAS*, 489, 3990. doi:10.1093/mnras/stz2423

- Rebassa-Mansergas, A., Maldonado, J., Raddi, R., et al. 2021, MNRAS, 505, 3165. doi:10.1093/mnras/stab1559
- Rebassa-Mansergas, A., Solano, E., Jiménez-Esteban, F. M., et al. 2021, MNRAS, 506, 5201. doi:10.1093/mnras/stab2039
- Ren, J. J., Rebassa-Mansergas, A., Luo, A. L., et al. 2014, A&A, 570, A107. doi:10.1051/0004-6361/201423689
- Ren, J.-J., Rebassa-Mansergas, A., Parsons, S. G., et al. 2018, MNRAS, 477, 4641. doi:10.1093/mnras/sty805
- Riello et al. 2021, A&A, 649, id.A3, 33 pp.
- Rogers, L. K., Bonsor, A., Xu, S., et al. 2024, MNRAS, 527, 6038. doi:10.1093/mnras/stad3557
- Sana, H., Le Bouquin, J.-B., Lacour, S., et al. 2014, ApJS, 215, 15. doi:10.1088/0067-0049/215/1/15
- Santos-García, A., Torres, S., Rebassa-Mansergas, A., et al. 2025, A&A, arXiv:2502.11593 [astro-ph.SR]
- Skrutskie, M. F., Cutri, R. M., Stiening, R., et al. 2006, AJ, 131, 1163. doi:10.1086/498708
- Sun, Y., Cheng, Z., Ye, S., et al. 2021, ApJS, 257, 65. doi:10.3847/1538-4365/ac283a
- Swan, A., Farihi, J., Su, K. Y. L., et al. 2024, MNRAS, 529, L41. doi:10.1093/mnras/ltad198
- Torres, S., García-Becerro, E., Isern, J. 1998, ApJ, 508, L71
- Vettigli, G. 2018, <https://github.com/JustGlowing/minisom/>
- Vincent, O., Barstow, M. A., Jordan, S., et al. 2024, A&A, 682, A5
- Wang, B. & Han, Z. 2012, NewAR, 56, 122. doi:10.1016/j.newar.2012.04.001
- Way, M., Klose, C. 2012, PASP, 124
- Willems, B. & Kolb, U. 2004, A&A, 419, 1057. doi:10.1051/0004-6361:20040085
- Wilson, T. G., Farihi, J., Gänsicke, B. T., et al. 2019, MNRAS, 487, 133. doi:10.1093/mnras/stz1050
- Winters, J. G., Henry, T. J., Jao, W.-C., et al. 2019, AJ, 157, 216. doi:10.3847/1538-3881/ab05dc
- Xu, S. & Jura, M. 2012, ApJ, 745, 88. doi:10.1088/0004-637X/745/1/88
- Zhao, J. K., Oswalt, T. D., Willson, L. A., et al. 2012, ApJ, 746, 144. doi:10.1088/0004-637X/746/2/144